Supporting Information

Interwoven Three-Dimensional Architecture of Cobalt Oxide Nanobrush-Graphene@$Ni_xCo_{2x}(OH)_{6x}$ for High-Performance Supercapacitors

Longbing Qu ,[†] Yunlong Zhao ,[†] [§]Aamir Minhas Khan,[†] Chunhua Han, *[†] Kalele Mulonda Hercule,[†] Mengyu Yan,[†] Xingyu Liu, [†] Wei Chen,[†] Dandan Wang,[†] Zhengyang Cai,[†] Wangwang Xu,[†] Kangning Zhao,[†] Xiaolin Zheng,[‡] Liqiang Mai*[†]

[†]State Key Laboratory of Advanced Technology for Materials Synthesis and Processing, Wuhan University of Technology, Wuhan 430070, China.

[‡]Department of Mechanical Engineering, Stanford University, Stanford, California 94305, United States.

[§]Department of Chemistry and Chemical Biology, Harvard University, Cambridge, Massachusetts 02138, USA.

This file includes:

1. Supplementary Figures

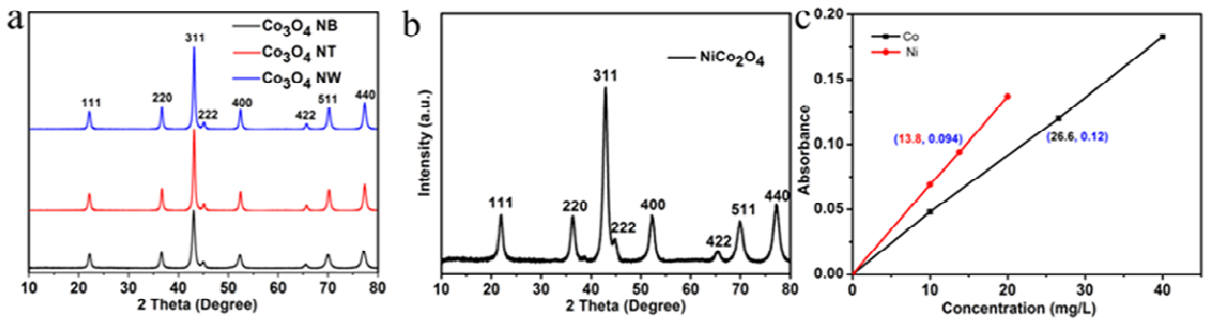

Figure S1. (a) XRD patterns of Co_3O_4 nanobrush (Co_3O_4 NB), Co_3O_4 nanotube (Co_3O_4 NT), Co_3O_4 nanowire (Co_3O_4 NW), respectively. (b) XRD pattern of $Ni_xCo_{2x}(OH)_{6x}$ (NCH) after calcination at 350 ℃ for 5 hours. (c) Atomic absorption spectrometry (AAS) results of Ni-Co hydroxides.

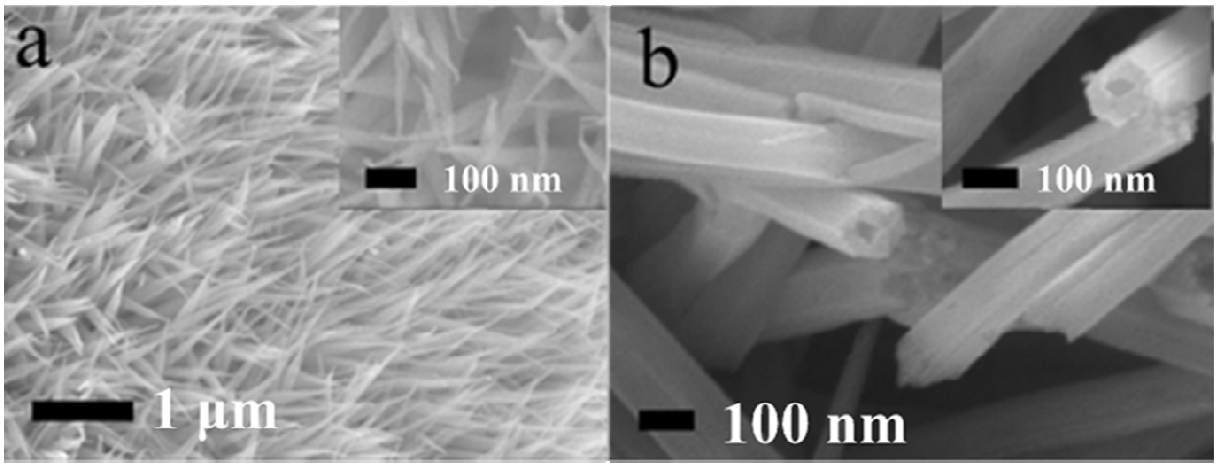

Figure S2. (a) SEM images of Co_3O_4 NW. (b) SEM images of Co_3O_4 NT.

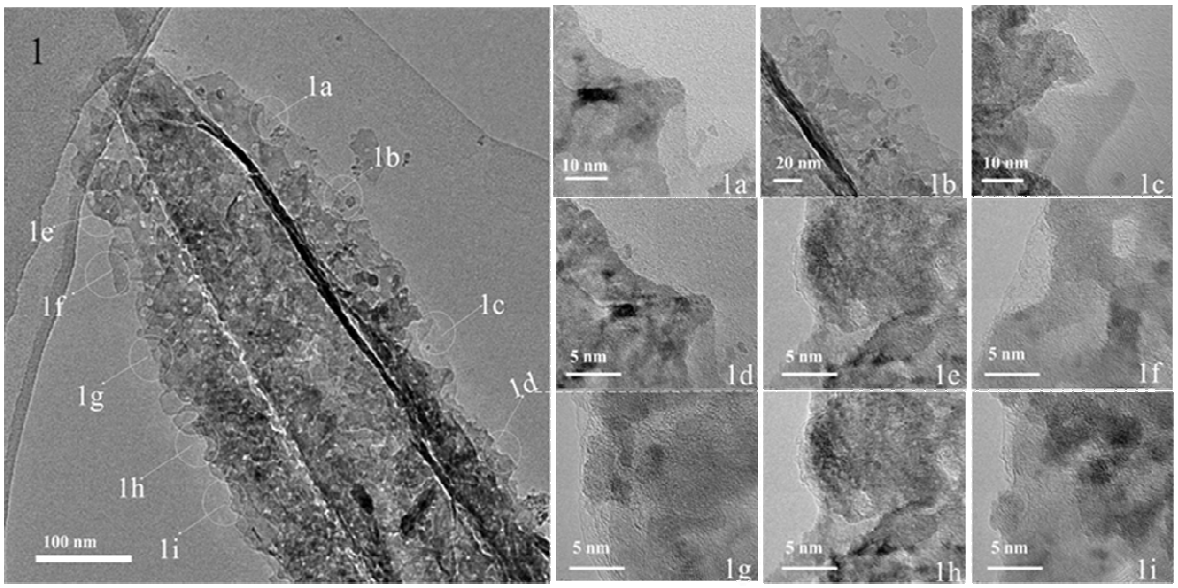

Figure S3. (1) TEM image of CNG (1); (1a-1i) Zoom-in TEM images of CNG of the different parts, respectively.

Figure S3 shows the high quality TEM image of cobalt oxide nanobrush-graphene to confirm that the whole surface of CN is fully (or connectively) covered by graphene film. As in the low magnification, it is not very obvious to see the graphene film on the surface of the CN (because the cobalt oxide nanobrush is composed with numbers of ultrathin nanosheet, the graphene film is also very thin, it is not very easy to identify the graphene on the surface of CN). So, we captured the high-magnification TEM images of the different parts of CNG, it clearly shows that all of these parts have the graphene film on the surface. Therefore, it confirms that the whole surface of CN is fully (or connectively) covered by thin graphene film.

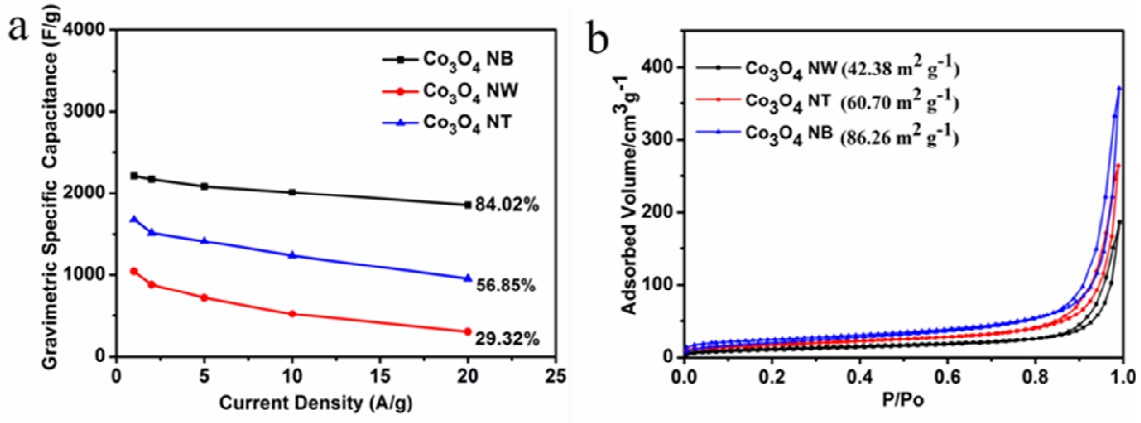

Figure S4. (a) Rate capability of Co_3O_4 NB, Co_3O_4 NT and Co_3O_4 NW respectively. (b) The nitrogen adsorption-desorption isotherms of the Co_3O_4 NB, Co_3O_4 NT and Co_3O_4 NW, respectively.

Figure S4a displays the rate capability of Co_3O_4 nanobrush (Co_3O_4 NB), Co_3O_4 nanowire (Co_3O_4 NW) and Co_3O_4 nanotube (Co_3O_4 NT). The Co_3O_4 NB exhibits a gravimetric capacitance decrease from 2209 F g^{-1} at 1 A g^{-1} to 1856 F g^{-1} at 20 A g^{-1} with 84.02% capacitance retention, which is much higher than those of Co_3O_4 NW (29.32%) and Co_3O_4 NT (56.85%). This is mainly because as pseudocapacitor the faradic reaction almost happens on or near the surface of the active materials, it requires the electrode material have very low diameter, high specific surface area and much more specific reactive sites directly connect with electrolyte. The present active material Co_3O_4 NB is connected by numbers of ultrathin nanosheets (about 15 nm in thickness), this morphology increase the ion diffusion OH^- (Figure S6a1), increases the specific surface reactive sites and makes Co_3O_4 reacted with LiOH electrolyte more quickly, thus leading to a much higher gravimetric specific capacitance and better rate capability than that of Co_3O_4 NW and Co_3O_4 NT, which is in agreement with the Brunauer-Emmett-Teller (BET) surface area (Figure S4b), cyclic voltammetry (CV) curves at 1 mV s^{-1} (Figure S5a) and electrochemical impedance spectra (EIS) (Figure S6a) of these three samples.

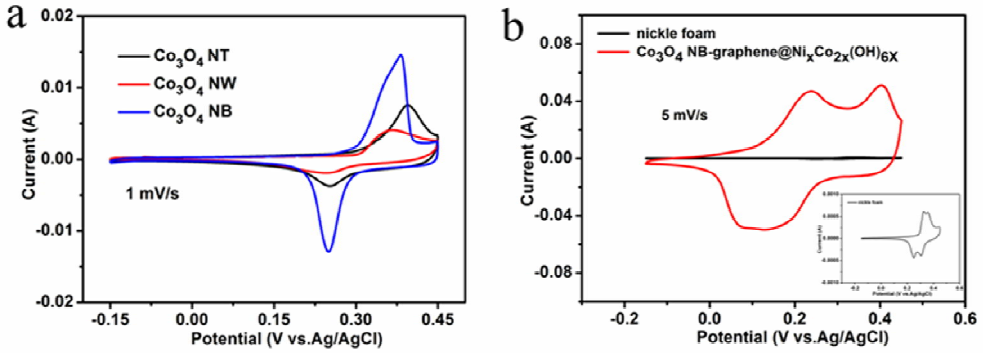

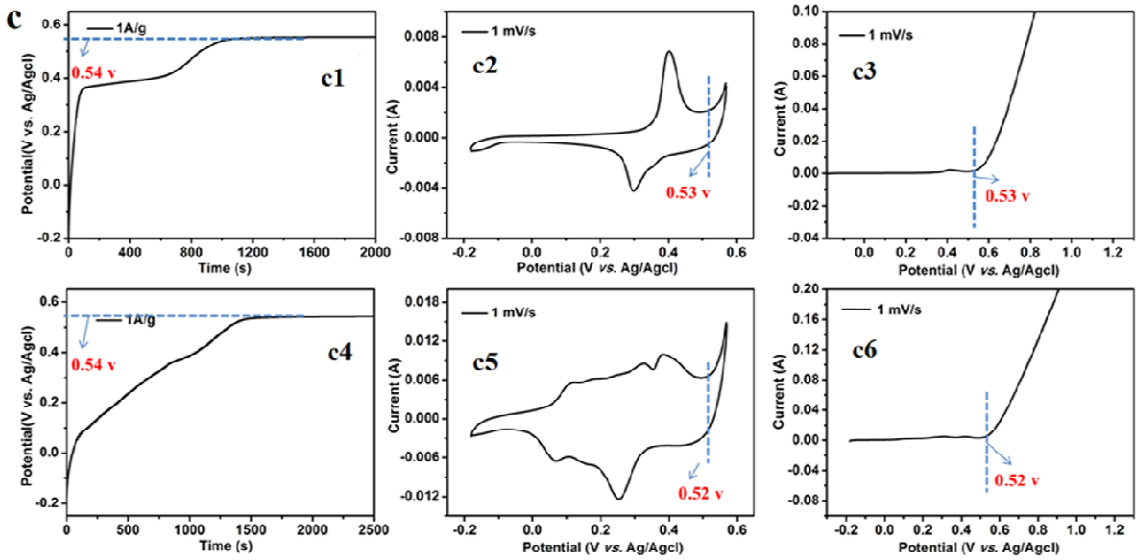

Figure S5. (a) CV curves of Co_3O_4 NB, Co_3O_4 NT, Co_3O_4 NW at the scan rate of 1 mV s^{-1}, respectively. (b) CV curves of the nickel foam and the 3D frame architecture electrode at the scan rate of 5 mV s^{-1} respectively. (c1) Charge curve of Co_3O_4 nanobrush at the current density of 1 A/g in 1 mol L^{-1} LiOH electrolyte. (c2) CV curves of Co_3O_4 nanobrush at the scan rate of 1 mV/S in 1 mol L^{-1} LiOH electrolyte. (c3) Water oxidation potential of the Co_3O_4 nanobrush at the scan rate of 1 mV/S in 1 mol L^{-1} LiOH electrolyte. (c4) Charge curve of interwoven 3D CNG@NCH at the current density of 1 A/g in 1 mol L^{-1} LiOH electrolyte. (c5) CV curves of interwoven 3D CNG@NCH at the scan rate of 1 mV/S in 1 mol L^{-1} LiOH electrolyte. (c6) Water oxidation potential of the interwoven 3D CNG@NCH at the scan rate of 1 mV/S in 1 mol L^{-1} LiOH electrolyte.

From Figure S5a, it clearly observes that the peak current of Co_3O_4 NB is much higher than that of Co_3O_4 NT and Co_3O_4 NW, which indicates that there are much more active materials reacted with OH^- at the same scan rate and active material mass loading level.

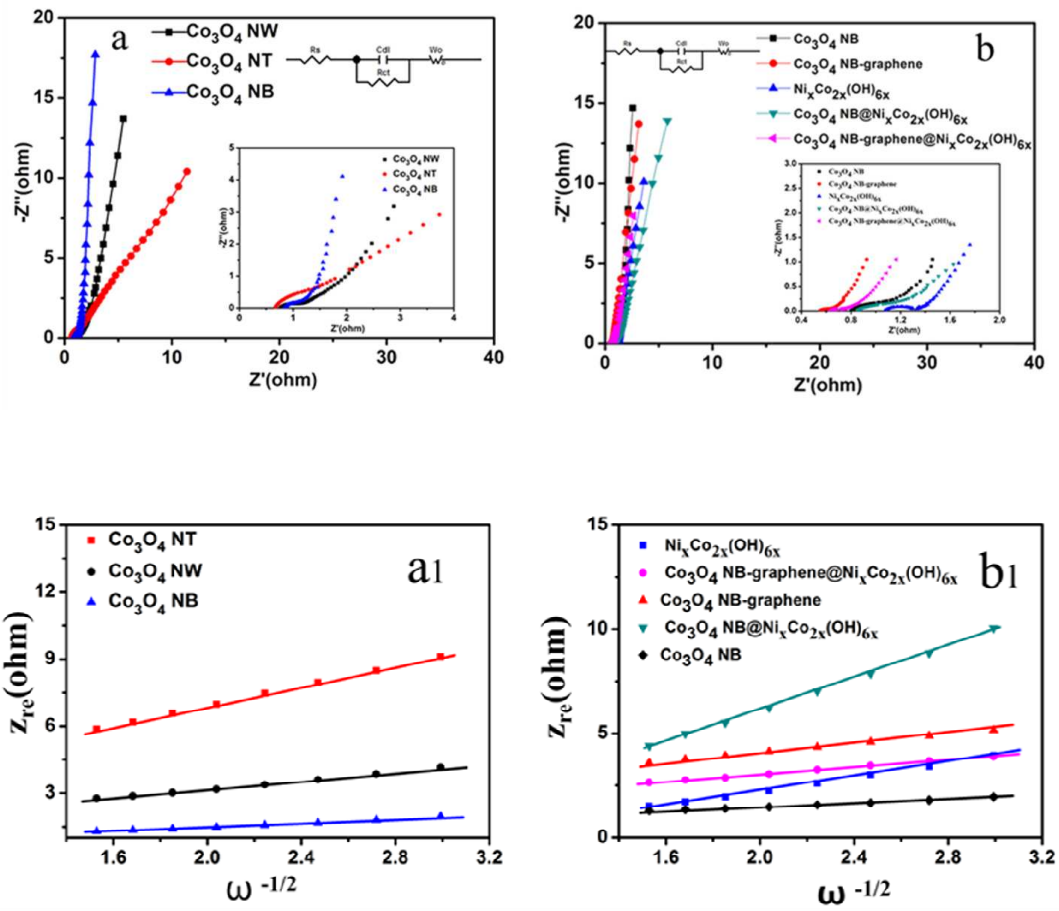

Figure S6. (a) An EIS Nyquist plots of Co_3O_4 NB, Co_3O_4 NT, Co_3O_4 NW in the frequency range of 0.1 Hz to 10^5 Hz at open current circuit. The inset is the expanded view. (b) An EIS Nyquist plots of CN, CNG, NCH, CN@NCH and CNG@NCH in the frequency range of 0.1 Hz to 10^5 Hz at open current circuit. The inset is the expanded view. For CN (R_s:0.8 Ω, R_{ct}:0.07 Ω), CNG, (R_s:0.54 Ω, R_{ct}:0.027 Ω), NCH (R_s:1.08 Ω, R_{ct}:0.18 Ω), CN@NCH, (R_s:0.85 Ω, R_{ct}:0.11 Ω), CNG@NCH, (R_s:0.63 Ω, R_{ct}:0.047 Ω). R_s: includes the inherent resistance of the electroactive material, ionic resistance of electrolyte and contact resistance at the interface between electrolyte and electrode. R_{ct}: charge transfer resistance. (a1) Variations and fittings between Z_{re} and the reciprocal square root of the angular frequency in the low frequency region of Co_3O_4 NB, Co_3O_4 NT, Co_3O_4 NW at open current circuit. (b1) Variations and fittings between Z_{re} and the reciprocal

square root of the angular frequency in the low frequency region of CN, CNG, NCH, CN@NCH and CNG@NCH at open current circuit.

The values of D_{OH^-} were calculated from the inclined lines in the Warburg region using the following equation : $D=R^2T^2/\ 2A^2n^4F^4C^2\sigma^2$ (1) (Ref. 1), where R is the gas constant, T is the absolute temperature, A is the surface area of the cathode electrode, n is the number of electrons per molecule during oxidization, F is the Faraday constant, C is the OH^- concentration (1×10^{-3} mol cm^{-3}), and σ is the Warburg factor associated with Zre ($Z\text{re} \propto \sigma\ \omega^{-1/2}$). After linear fitting the relation plot between Zre and the reciprocal square root of the angular frequency (as shown in Figure S6a1), The Warburg factor of Co_3O_4 NB is lower than that of Co_3O_4 NT and Co_3O_4 NW, according to equation (1), it indicates that the Co_3O_4 NB has much faster ion diffusion. From Figure S6b1, we can observe that the Warburg factor of CNG@NCH is almost equal to that of CN and CNG, which indicates that electrodeposition of NCH nanofiake interweaved with CNG does not retard the ion diffusion.

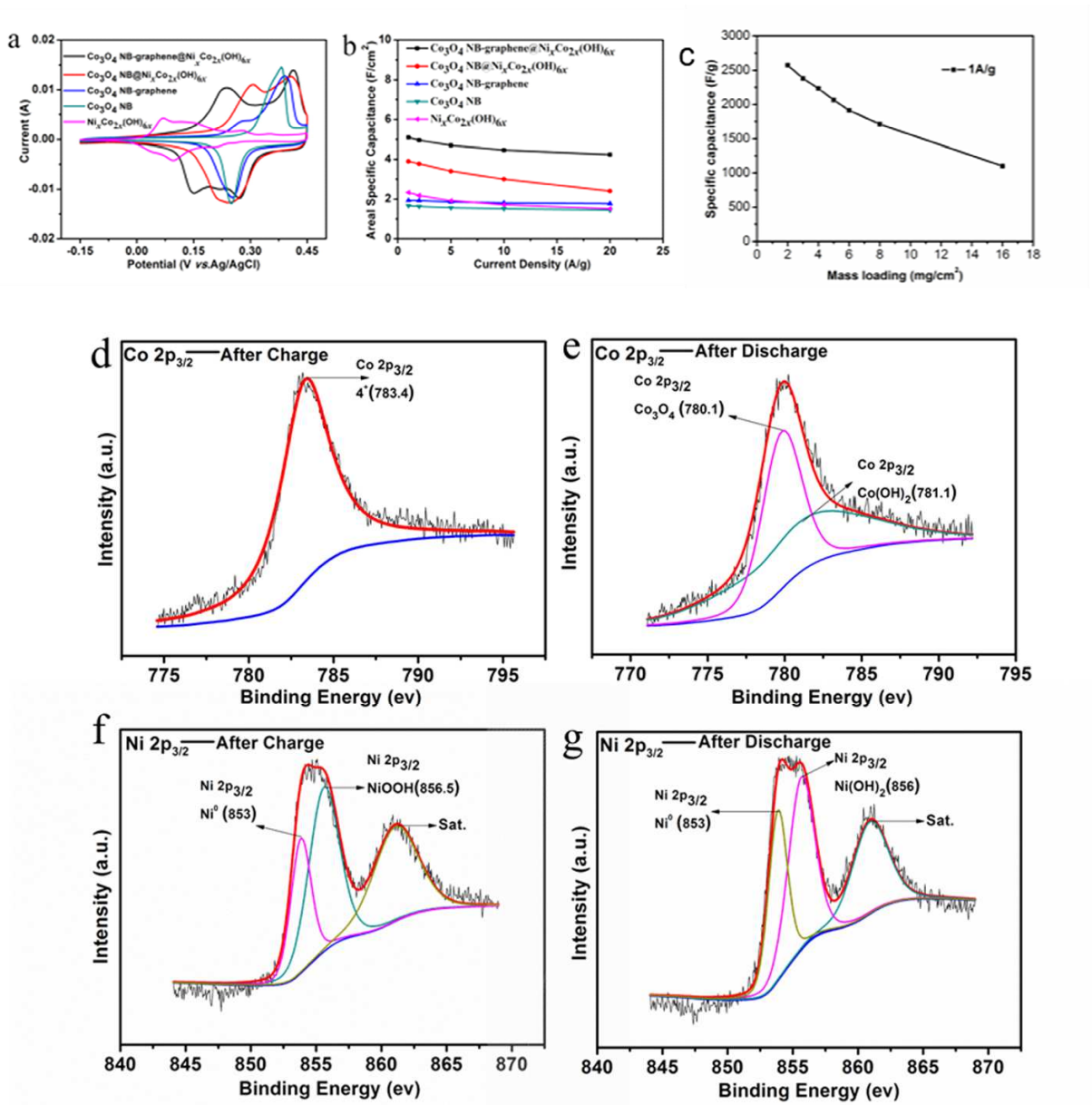

Figure S7. (a) CV curves of CN, CNG, NCH, CN@NCH and CNG@NCH at a scan rate of 1 mV s^{-1} in 1 M LiOH, respectively. (b) Areal specific capacitances of CN, CNG, NCH, CN@NCH and CNG@NCH at different current densities, respectively. (c) Specific capacitances of our interwoven 3D frame electrode (CNG@NCH) with different mass loading on nickle foam. Co 2p XPS of our interwoven 3D CNG@NCH electrode after charge (d) and discharge (e). Ni 2p XPS of our interwoven 3D CNG@NCH electrode after charge (f) and discharge (g).

From Figure S7a, for CN, one pair of well-defined redox peaks with -0.15-0.45 V

(*vs*.Ag/AgCl) are visible which is due to the Co^{3+}/Co^{4+} reaction, [2] while two anodic peaks and one cathodic peak are found for CNG, which indicates more complete faradic reaction of CNG. Moreover from the CV curves, we also can see that the CV internal area of CNG is larger than that of CN, which indicates higher capacitance of CNG than that of CN. The CV curve of NCH presents three pairs of redox peaks. Two pairs of peaks are attributed to the faradic reactions related to $Co(OH)_2$/CoOOH and CoOOH/CoO_2, the other one pair of peaks are due to $Ni(OH)_2$/NiOOH.[3] Additionally, we also took the X-ray photoelectron spectroscopy (XPS) tests of our interwoven 3D CNG@NCH electrode after charge and discharge to further demonstrate the reaction mechanism of Co_3O_4 and nickle-cobalt hydroxides. The results show that the oxidation states of Co are Co^{4+} after charge and Co^{2+}, Co^{3+} after discharge, the oxidation states of Ni are Ni^{3+} after charge and Ni^{2+} after discharge, the existence of Ni^0 is ascribed to the nickle foam. [4, 5] All of these results indicate that the reaction mechanism of our interwoven 3D CNG@NCH electrode is corresponding very well with the literatures that have been reported before.[2, 3] Particularly, it should be noted that after the electrodeposition of NCH, the CV curve of the hierarchical nanostructured CN@NCH is obviously expanded, exhibiting a much higher areal capacitance compared with CN. For the final product CNG@NCH, three reduction peaks are observed, indicating that our 3D frame architecture electrode can very effectively make each component do the contribution to the total capacitance. The emergence of two pairs of broad peaks for the final 3D active material results from the superposition of the peaks of CNG and NCH. [6]

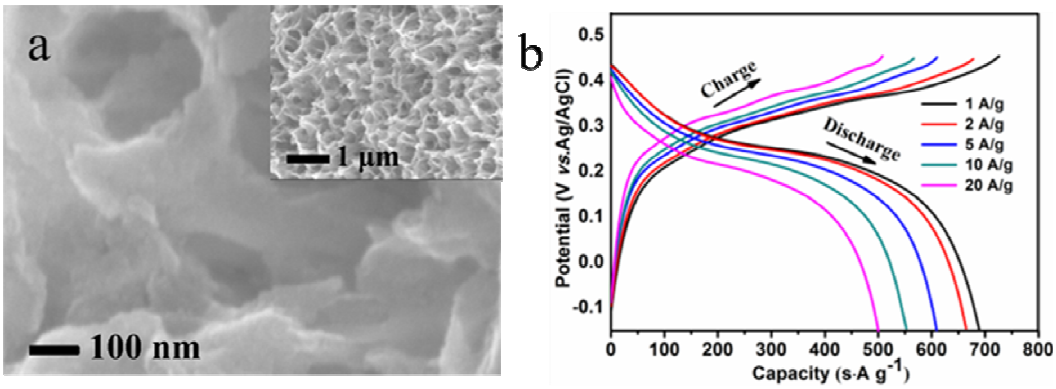

Figure S8. (a) SEM images of the hybrid electrode which the NCH is coated on the surface of CNG. (b) Charge and discharge curves of the hybrid electrode which the NCH is coated on the surface of CNG at different current densities.

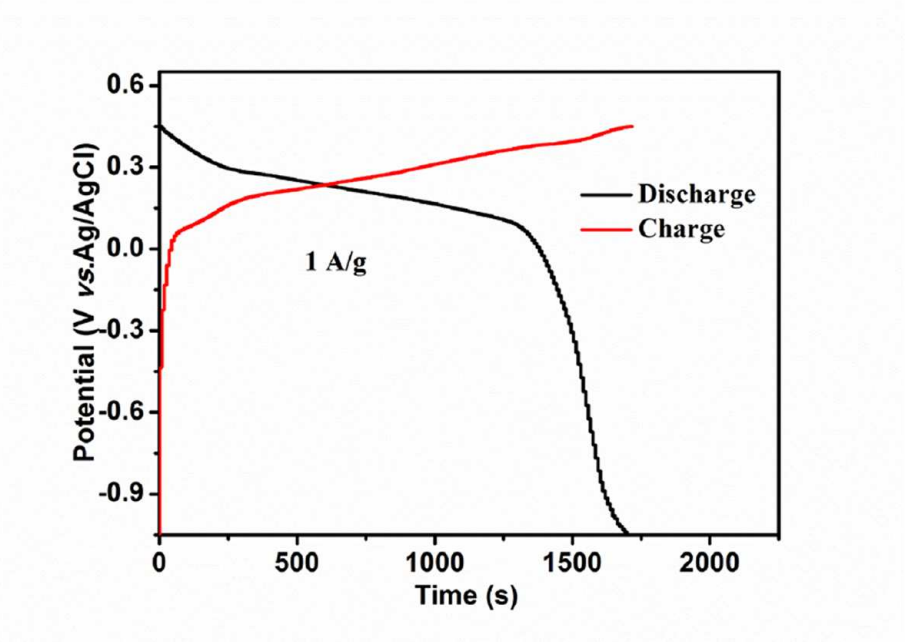

Figure S9. Charge and discharge curves of the 3D frame architecture electrode at the current density of 1 A/g.

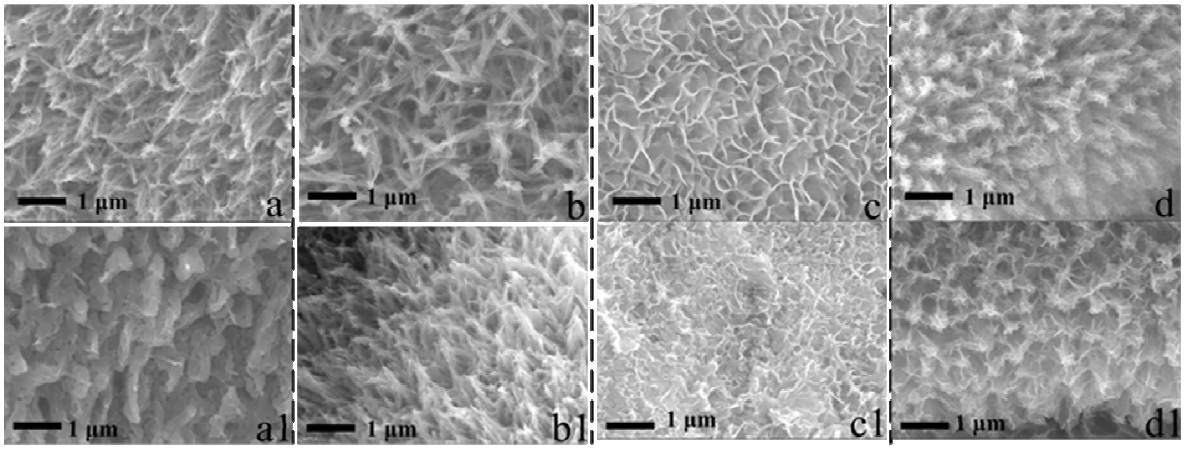

Figure S10. (a-d) SEM images CN (a), CNG (b), NCH (c) and CNG@NCH (d) electrodes before first cycle, respectively. a1-d1) SEM images CN (a1), CNG (b1), NCH (c1) and CNG@NCH (d1) electrodes after 5000 cycles at 20 A g-1, respectively.

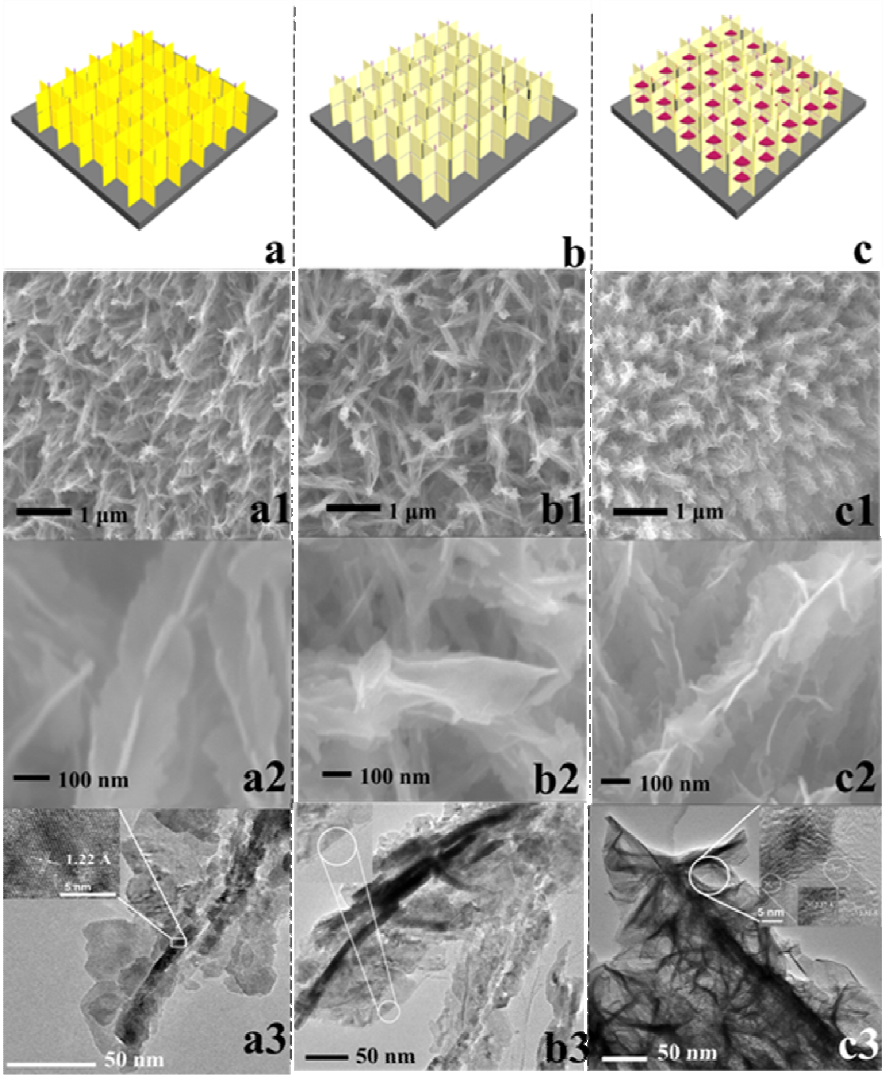

Figure S11. (a-c) Illustrated images of CN (a), CNG (b), and CNG@NCH (c), respectively. (a1-c1) SEM images of CN (a1), CNG (b1), and CNG@NCH (c1), respectively. (a2-c2) High-magnification images of CN (a2), CNG (b2), and CNG@NCH (c2), respectively. (a3-c3) TEM images of CN (a3), CNG (b3), and CNG@NCH (c3), respectively. The inset of a3 and c3 show the HRTEM of CN and CNG@NCH, respectively.

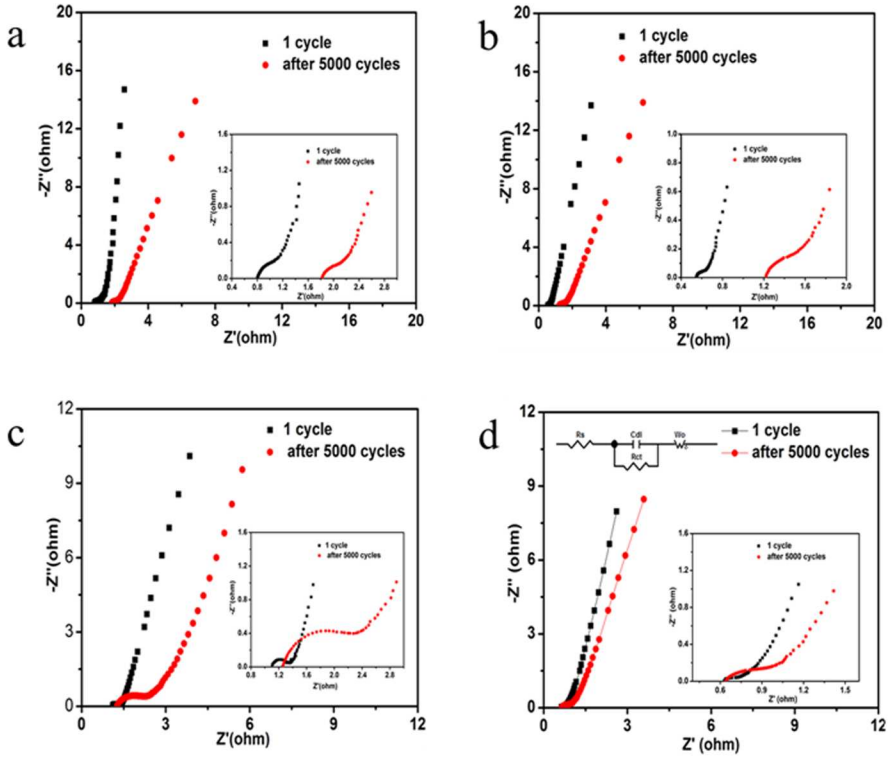

Figure S12. (a-d) An EIS Nyquist plots of CN (a), CNG (b), NCH (c) and CNG@NCH (d) electrodes after 5000 cycles at 20 A g^{-1} in the frequency range of 0.1 Hz to 10^5 Hz at open current circuit. The inset is the expanded view.

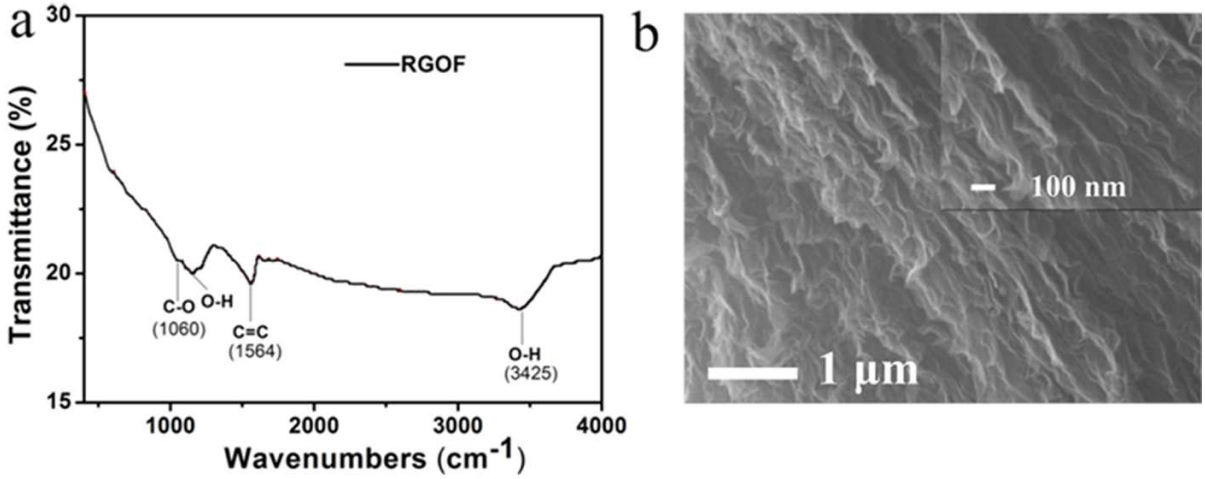

Figure S13. (a) FTIR spectrum of RGOF. (b) SEM images of RGOF. The inset shows the high-magnification of RGOF.

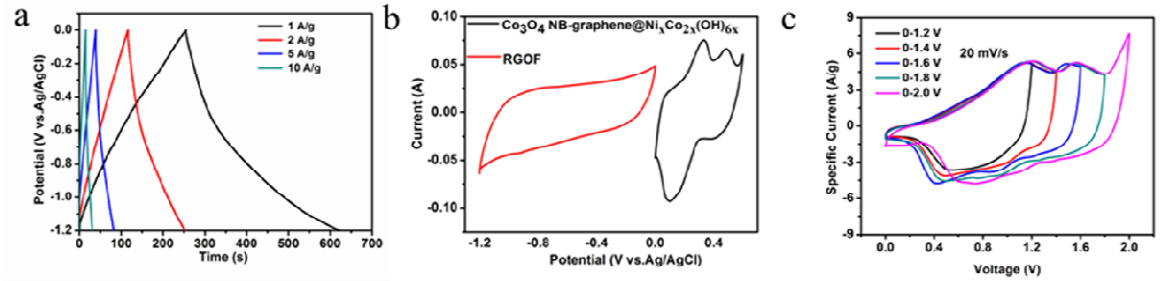

Figure S14. (a) Charge and discharge curves of RGOF electrode at different current densities. (Current densities vary from 1 A g^{-1} to 10 A g^{-1}). (b) CV curves of the RGOF (negative) and CNG@NCH (positive) electrodes at a same scan rate of 10 mV s^{-1}. (c) CV curves of the CNG@NCH//RGOF asymmetric supercapacitor measured at different potential windows at a scan rate of 20 mV s^{-1}.

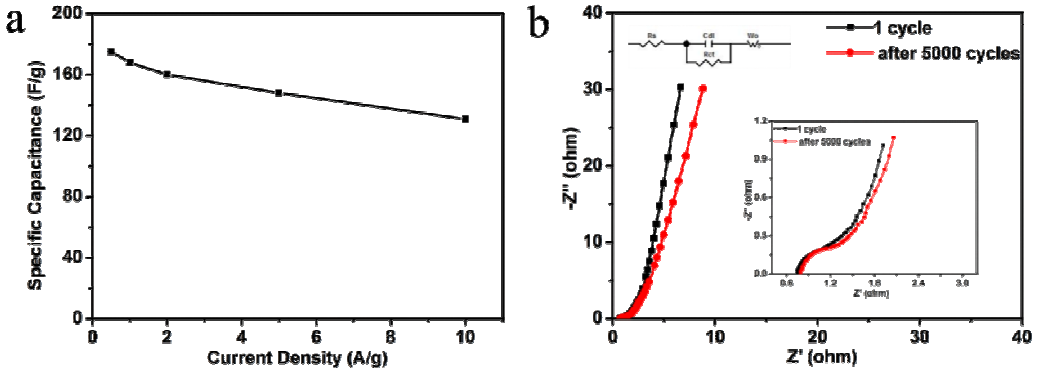

Figure S15. (a) Rate capability of CNG@NCH//RGOF asymmetric supercapacitor. (b) Nyquist plots of the first and 5000th cycle for the asymmetric supercapacitor in the frequency range from 0.01 Hz to 10^5 Hz at open current circuit. The inset is the expanded view.

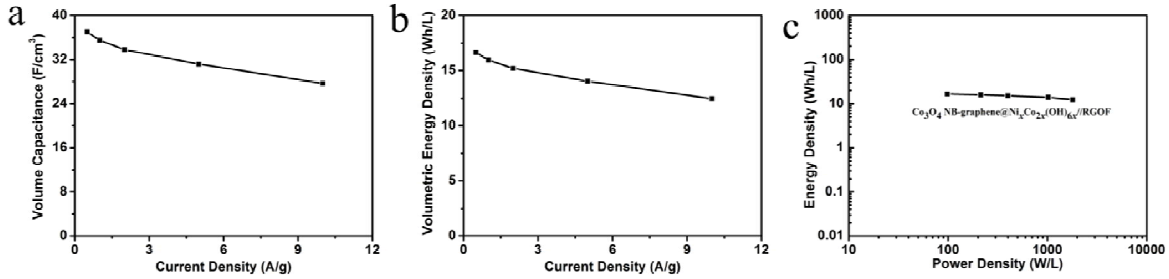

Figure S16. (a) Specific volumetric capacitance of CNG@NCH//RGOF asymmetric supercapacitor at different current densities. (b) Volumetric energy densities of our CNG@NCH//RGOF asymmetric supercapacitor at different current densities. (c) Ragone plot of our CNG@NCH//RGOF asymmetric supercapacitor.

2. Supplementary Tables

Table S1. The electrochemical performance of CN, CNG, Graphene, NCH, CN@NCH and CNG@NCH, respectively.

samples	Capacitance (F/g at 1A/g)	Capacitance (F/cm^2 at 1A/g)	capacitance retention (1A/g vs. 20A/g)	capacitance retention (after 5000 cycles)	mass of active materials (mg/cm^2)
Co_3O_4 nanobrush (CN)	2209	1.66	84.02%	52.6%	0.75
Co_3O_4 nanobrush-graphene(CNG)	2579	1.93	91.31%	63.9%	0.75
Graphene on nick foam	105	0.21			2.0
Nickle-cobalt hydroxides (NCH)	1650	2.06	48.63%	69.1%	1.25
CN@NCH	1947	3.9	61.7%		2.0
CNG@NCH	2550	5.1	82.98%	92.7%	2.0

Table S2. The electrochemical performance of various electrode materials.

Electrode materials	Gravimetric capacitance(F g^{-1})	Areal capacitance(F cm^{-2})	Reference
$CoMoO_4$–3D graphene (0.5 mg/cm^2)	2741 (1.43 A g^{-1}) 1488 (22.85 A g^{-1})	1.41 (1.43 A g^{-1}) 0.76 (22.85 A g^{-1})	[7]
3D hierarchical Co_3O_4 twin-spheres	751 (1 A g^{-1}) 611 (8 A g^{-1})		[8]
Co_3O_4 nanowire@ MnO_2 nanosheet (1.5 mg/cm^2)	487 (2.67 A g^{-1})	0.7 (4 mA cm^{-2})	[9]
Amorphous $Ni(OH)_2$ nanospheres (0.12 mg/cm^2)	2188 (1 mV s^{-1})	0.263(1 mV s^{-1})	[10]
	1250 (20 mV s^{-1})	0.15 (20 mV s^{-1})	
$Co_{0.67}Ni_{0.33}$ DHs/$NiCo_2O_4$/CFP (1.0 mg/cm^2)	1640 (2 mA cm^{-2})	1.64 (2 mA cm^{-2})	[3]
3D CoO@Polypyrrole (1.98 mg/cm^2)	2223 (1 mA cm^{-2}) 895 (20 mA cm^{-2})	4.43 (1 mA cm^{-2}) 1.79 (20 mA cm^{-2})	[11]
Co_3O_4/NiO core/shell (3.0 mg/cm^2)	853 (2 A g^{-1})	2.56 (2 A g^{-1})	[12]
Porous carbon spheres (0.46 mg/cm^2)	946 (20 A g^{-1})	0.44 (20 A g^{-1})	[13]
CNG@NCH (2.0 mg/cm^2)	2550 (1 A g^{-1}) 2116 (20 A g^{-1})	5.1 (1 A g^{-1}) 4.23 (20 A g^{-1})	Our work

Table S3. The maximum energy density of various asymmetric supercapacitors.

Capacitor	Energy density (Wh kg^{-1})	Reference
Amorphous $Ni(OH)_2$//active carbon (AC)	35.7	[10]
CoO@PPy//AC	43.5	[11]
$Ni(OH)_2$/ultrathin-graphite foam(UGF)// activated microwave exfoliated graphite oxide (a-MEGO)	44.0	[14]
A MnO_2 nanowire/graphene//graphene	30.4	[15]
$Ni(OH)_2$/carbon nanotube (CNT)//AC	50.6	[16]
Bacterial cellulose pellicles(*p*-BC) @MnO_2-2h// nitrogen-doped *p*-BC-5M	32.91	[17]
Co_3O_4@$Ni(OH)_2$//RGO	41.90	[18]
Co_3O_4NB-graphene@$Ni_xCo_{2x}(OH)_{6X}$// RGOF	78.75	Our work

3. Supplementary Methods

Preparation of cobalt oxide nanowire arrays on the nickel foam: 0.582 g $Co(NO_3)_2 \cdot 6H_2O$ and 0.6 g urea were dissolved in 70 ml deionized water to form homogeneous pink solution. Then solution was transferred into a 100 ml Teflon-lined stainless steel autoclave lines with a piece of clean nickel foam (20 mm*60 mm*0.4 mm) immersed into the reaction solution. The autoclave was sealed and maintained at 100 ℃ for 10 hours, and then cooled down to room temperature. The as synthesized samples were taken out, ultrasonically cleaned at 40 Hz for 5 minutes in the distilled water and rinsed with ethanol for several times, dried at 70 ℃ for 10 hours, annealed at 450 ℃ in Ar gas for 5 hours, then 300 ℃ in air for 5 hours.

Preparation of cobalt oxide nanotubes on the nickel foam: 0.582 g $Co(NO_3)_2 \cdot 6H_2O$ and 0.6 g urea were dissolved in 70 ml deionized water to form homogeneous pink solution. Then solution was transferred into a 100 ml Teflon-lined stainless steel autoclave lines with a piece of clean nickel foam (20 mm*60 mm*0.4 mm) immersed into the reaction solution. The autoclave was sealed and maintained at 100 ℃ for 10 h, and then cooled down to room temperature. The as synthesized samples were taken out, ultrasonically cleaned at 40 Hz for 5 minutes in the distilled water and rinsed with ethanol for several times, dried at 70 ℃ for 10 hours, annealed at 300 ℃ in air for 3 hours, then etched with 0.05 M HCl for 5 minutes.

4. Calculation of the Theoretical Capacitance

As the theoretical capacitance of pseudocapacitive materials are calculated by using the following formula: $C=n\times F/(\Delta V\times M)$, where n is the moles of charge transferred per mole of pseudocapacitive materials , F is Faraday's constant (96485.3383 C mol^{-1}), M is the molar mass of the pseudocapacitive materials and ΔV is the potential sweep range. [11] In our present work, our pseudocapacitive materials is Co_3O_4-graphene@$Ni_xCo_{2x}(OH)_{6x}$, in this situation, we can

suppose that the X is 1, so we regard our materials as Co_3O_4-graphene@$NiCo_2(OH)_6$. The mass of the graphene is very little which is less than 0.05 mg and it is not serving as the pseudocapacitive materials. We calculated the theoretical capacitance of Co_3O_4 and $NiCo_2(OH)_6$ are 2680 F/g and 2892 F/g, respectively with the potential sweep range of 0.6 V. (Our CNG electrode has a specific capacitance of 2579 F/g at a current density of 1A/g, which is very close to the theoretical capacitance of Co_3O_4). The mass of Co_3O_4 is 0.75 mg/cm^2, the mass of $NiCo_2(OH)_6$ is 1.25 mg/cm^2. Based on all of these, we calculated the theoretical capacitance of CNG@NCH is 2812 F/g at the potential sweep range of 0.6 V (Our interwoven 3D frame architecture electrode CNG@NCH has a specific capacitance of 2550 F g^{-1} at 1 A g^{-1}, which is very close to the theoretical capacitance of CNG@NCH at the potential sweep range of 0.6V).

REFERENCES

(1) Wu, X. L.; Guo, Y. G.; Su, J.; Xiong, J. W.; Zhang, Y. L.; Wan, L. J. *Adv. Energy Mater.* **2013**, 3, 1155.

(2) Casella, I. G.; Gatta, M. *J. Electro. Chem.* **2002**, 534, 31.

(3) Huang, L.; Chen, D. C.; Ding, Y.; Feng, S.; Wang, Z. L.; Liu, M. L. *Nano Lett.* **2013**, 13, 3135.

(4) Higuchi, E.; Otsuka, H.; Chiku, M.; Inoue, H. *J. Power Sources.* **2014**, 248, 762.

(5) Chang, Y,; Hau, Y.; Liu, C.; Huang, Y.; Li, C.; Shih, K.; Feng, S. *Nanoscale.* **2014**, 6, 15309.

(6) Shang, C. Q.; Dong, S. M.; Wang, S.; Xiao, D. D.; Han, P. X.; Wang, X. G.; Gu, L.; Cui, G. L. *ACS Nano.* **2013**, 7, 5430.

(7) Yu, X.; Lu, B.; Xu, Z. *Adv. Mater*. **2013**.

(8) Xiao, Y. H.; Liu, S. J.; Li, F.; Zhang, A. Q.; Zhao, J. H.; Fang, S. M.; Jia, D. Z. *Adv. Funct.*

Mater. **2012**, 22, 4052.

(9) Liu, J. P.; Jiang, J.; Cheng, C. W.; Li, H. X.; Zhang, J. X.; Gong, H.; Fan, H. J. *Adv. Mater.* **2011**, 23, 2076.

(10) Li, H. B.; Yu, M. H.; Wang, F. X.; Liu, P.; Liang, Y.; Xiao, J.; Wang, C. X.; Tong, Y. X.; Yang, G. W. *Nat. commun*. **2013**, 4, 1894.

(11) Zhou, C.; Zhang, Y.; Li, Y.; Liu, J. P. *Nano Lett.* **2013**, 13, 2078.

(12) Xia, X. H.; Tu, J. P.; Zhang, Y. Q.; Wang, X. L.; Gu, C. D.; Zhao, X.-B.; Fan, H. J. *ACS Nano*

2012, **6**, 5531.

(13) Mai, L. Q.; Khan, A. M.; Tian, X. C.; Hercule, K. M.; Zhao, Y. L.; Xu, L.; Xu, X. *Nat. Commun.* **2013**, 4, 2923.

(14) Ji, J. Y.; Zhang, L. L.; Ji, H. X. Y.; Li, Zhao, X.; Bai, X,; Fan, X. B.; Zhang, F. B.; Ruoff, R. S. *ACS Nano.* **2013**, 7, 6242.

(15) Wu, Z. S.; Ren, W C.; Wang, D. W.; Li, F.; Liu, B. L.; Cheng, H.-M. *ACS Nano.* **2010**, 4, 5835.

(16) Tang, Z.; Tang, C. h.; Gong, H. *Adv. Funct. Mater.* **2012**, 22, 1272-1278.

(17) Chen, L. F.; Huang, Z. H.; Liang, H. W.; Guan, Q. F.; Yu, S. H. *Adv. Mater.* **2013**, 25, 4746.

(18) Tang, C. h.; Yin, X.; Gong, H. *ACS Appl. mater. Interfaces*. **2013**, 5, 10574.